



Mixed finite elements for numerical weather prediction

C.J. Cotter^{*}, J. Shipton

Department of Aeronautics, Imperial College London, South Kensington Campus, London SW7 2AZ, United Kingdom

ARTICLE INFO

Article history:

Received 14 November 2011

Received in revised form 8 May 2012

Accepted 10 May 2012

Available online 9 June 2012

Keywords:

Mixed finite elements

Stability

Steady geostrophic states

Geophysical fluid dynamics

Numerical weather prediction

ABSTRACT

We show how mixed finite element methods that satisfy the conditions of finite element exterior calculus can be used for the horizontal discretisation of dynamical cores for numerical weather prediction on pseudo-uniform grids. This family of mixed finite element methods can be thought of in the numerical weather prediction context as a generalisation of the popular polygonal C-grid finite difference methods. There are a few major advantages: the mixed finite element methods do not require an orthogonal grid, and they allow a degree of flexibility that can be exploited to ensure an appropriate ratio between the velocity and pressure degrees of freedom so as to avoid spurious mode branches in the numerical dispersion relation. These methods preserve several properties of the C-grid method when applied to linear barotropic wave propagation, namely: (a) energy conservation, (b) mass conservation, (c) no spurious pressure modes, and (d) steady geostrophic modes on the f -plane. We explain how these properties are preserved, and describe two examples that can be used on pseudo-uniform grids: the recently-developed modified RTk-Q(k-1) element pairs on quadrilaterals and the BDFM1- $P1_{DG}$ element pair on triangles. All of these mixed finite element methods have an exact 2:1 ratio of velocity degrees of freedom to pressure degrees of freedom. Finally we illustrate the properties with some numerical examples.

© 2012 Elsevier Inc. All rights reserved.

1. Introduction

There are a number of groups that have been developing dynamical cores for numerical weather prediction (NWP) and climate modelling, based on triangular meshes on the sphere or on the dual meshes composed of hexagons together with a small number of hexagons [22,20,25]. The principal reason for adopting these grids is that they provide a direct addressing data structure whilst avoiding the polar singularity of the latitude-longitude grid, which introduces a bottleneck to scaling on massively parallel architectures due to the convergence of meridians. One approach to developing numerical discretisations on triangular or hexagonal grids is to adapt the staggered Arakawa C-grid finite difference method on quadrilaterals [1] (used in several currently operational NWP models, such as the UK Met Office Unified Model [15]) since this type of staggering prevents pressure modes (non-constant functions on the pressure grid that have zero numerical gradient). By defining discrete curl and divergence operators which satisfy $\nabla \times \nabla \cdot = 0$, it is possible to construct C-grid discretisations for horizontal wave propagation which have stationary geostrophic modes on the f -plane [28], a necessary condition for accurate representation of geostrophic adjustment processes. These operators can be used to construct energy and enstrophy C-grid discretisations for the nonlinear rotating shallow-water equations using the vector invariant form [23]. The drawback with using the C-grid finite difference method on triangles or hexagons instead of quadrilaterals is that the ratio of velocity and pressure degrees of freedom (DOF) is altered. The quadrilateral C-grid has one pressure DOF stored at the centre of each grid

^{*} Corresponding author.

E-mail address: colin.cotter@imperial.ac.uk (C.J. Cotter).

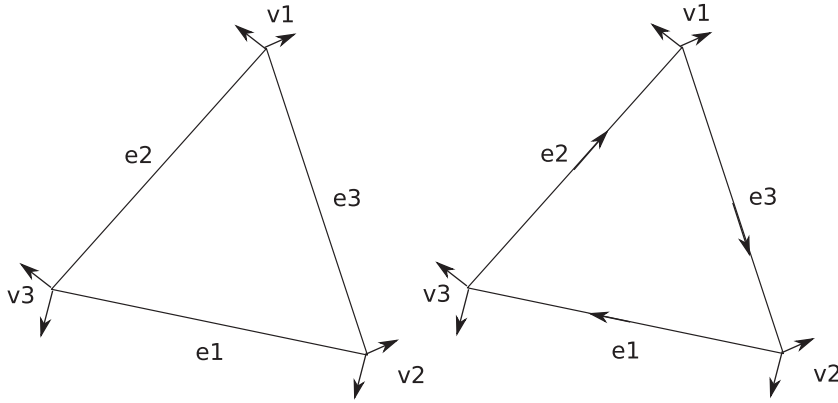


Fig. 1. Diagram showing degrees of freedom in (left) BDM1 vector element, (right) augmented BDM1 vector element.

cell, and two velocity DOF per grid cell (normal velocity is stored at each of the four edges, which are each shared with the neighbouring cell on the other side of the face).¹ This is considered the ideal ratio, since the velocity then has an equal number of rotational and divergent DOF which are coupled together in the correct way so that there are two inertia-gravity modes (the inward and outward propagating modes) for each Rossby mode. On the other hand, the triangular C-grid has only 3/2 velocity DOF per grid cell, and the hexagonal C-grid has 3 velocity DOF per grid cell. This means that the triangular C-grid has four inertia-gravity modes per Rossby mode; the extra spurious inertia-gravity branch has a frequency range that decreases with Rossby deformation radius, leading to “checkerboard patterns” in the divergence when the deformation radius is small (as it can be in the ocean, or when there are many vertical layers). The hexagonal C-grid has an equal number of inertia-gravity and Rossby modes; the extra spurious Rossby mode has very low frequencies and propagates Eastwards on the β -plane ([27]). The effects of these spurious Rossby modes has not been reported in practice but there are concerns amongst the operational NWP community that if spurious modes are supported by the grid, then they might be initialised during the data assimilation process or by physics parameterisations [26]. It may also be the case that the spurious modes lead to spurious spread/lack of spread in ensemble forecasts. Careful numerical experiments are required to investigate this concern.

The finite element method provides the opportunity to alter the number of degrees of freedom per triangular element to ameliorate this problem. A number of finite element pairs on triangles have been proposed for geophysical fluid dynamics, mostly in the ocean modelling community [29,19,18,13,11,17]. In [24], the lowest order Brezzi–Douglas–Marini element pair [9], known as BDM1, was investigated in the context of the discrete shallow-water equations. The velocity space is piecewise linear with continuous normal components, and the pressure space is piecewise constant. The natural data structure for the velocity space stores two normal velocity components on each edge, and hence there are 3 velocity DOF per triangular element and 1 pressure DOF. There are too many velocity DOF and hence there will be too many Rossby modes per inertia-gravity mode, just as for the hexagonal C-grid.

In this paper we examine the application of finite element pairs that fall within the framework of finite element exterior calculus [4]. This includes the BDM1-P0 element pair as an example, but we shall be advocating other choices that have a more favourable balance of velocity and pressure DOFs. The key result of this paper is in showing that discretisations of the linear rotating shallow water equations on the f -plane constructed using these finite element pairs on arbitrary meshes satisfy a crucial property, namely that geostrophic modes are exactly steady. This is achieved by making use of the discrete Helmholtz decomposition. As described in [2], existence of such a decomposition requires that the following diagram commutes:

$$\begin{array}{ccccc}
 H^1(\Omega) & \xrightarrow{\nabla^\perp} & H(\text{div}, \Omega) & \xrightarrow{\nabla \cdot} & L_2(\Omega) \\
 \downarrow \Pi^E & & \downarrow \Pi^S & & \downarrow \Pi^V \\
 E & \xrightarrow{\nabla^\perp} & S & \xrightarrow{\nabla \cdot} & V
 \end{array} \tag{1}$$

where Π^E , Π^S and Π^V are suitably chosen projection operators. The same Helmholtz decomposition can then be used to study the discrete dispersion relations for the numerical discretisation. Within this framework, we then conclude that an optimal choice is to have $\dim(S) = 2\dim(V)$ which, at least in the periodic plane, satisfies necessary conditions for absence of both spurious inertia-gravity and spurious Rossby waves. This motivates the use of finite element pairs that meet this criteria, which includes the RT($k+1$)-Q k family on quadrilaterals and the BDFM1-P1_{DG} pair on triangles.

The rest of this paper is organised as follows. The general framework of mixed finite element methods applied to the linear rotating shallow-water equations is described in Fig. 5, and the four properties of energy conservation, local mass

¹ Here, and in the rest of the paper, we consider compact domains without boundary such as the sphere and rectangles with double periodic boundary conditions.

conservation, absence of spurious pressure modes and steady geostrophic modes are discussed. In Section 3, two examples are then introduced that fit into this framework, and numerical results are presented in Section 4. Finally, we give a summary and outlook in Section 5.

2. Mixed finite elements for geophysical fluid dynamics

In this section we describe how mixed finite elements can be used to build flexible discretisations on pseudouniform grids. We concentrate on the rotating shallow-water equations which are regarded in the numerical weather prediction community as being a simplified model that contains many of the issues arising in the horizontal discretisation for dynamical cores. Since in this paper we are concerned with wave propagation properties, we restrict attention to the linearised equations on the f -plane, β -plane or the sphere. First, we introduce the mixed finite element formulation applied to the linear rotating shallow-water equations, then we discuss various properties of the formulation that are a requirement for numerical weather prediction applications, namely global energy and local mass conservation, absence of spurious pressure modes and steady geostrophic states. These properties all rely on exact sequence properties, i.e., div-curl relations, as described in [4].

2.1. Spatial discretisation of the linear rotating shallow-water equations

In this paper we consider the discretisation of the linear rotating shallow-water equations on a two dimensional surface Ω that is embedded in three dimensions (which we restrict to be compact with no boundaries, e.g. the sphere or double periodic x - y plane):

$$\mathbf{u}_t + f\mathbf{u}^\perp + c^2\nabla\eta = 0, \quad \eta_t + \nabla \cdot \mathbf{u} = 0, \quad \mathbf{u} \cdot \mathbf{n} = 0 \quad \text{on } \partial\Omega, \quad (2)$$

where $\mathbf{u} = (u, v)$ is the horizontal velocity, $\mathbf{u}^\perp = \mathbf{k} \times \mathbf{u}$, f is the Coriolis parameter, $c^2 = gH$, g is the gravitational acceleration, H is the mean layer thickness, and $h = H(1 + \eta)$ is the layer thickness, \mathbf{k} is the normal to the surface Ω , and ∇ and $\nabla \cdot$ are appropriate invariant gradient and divergence operators defined on the surface. We form the finite element approximation by multiplying by time-independent test functions \mathbf{w} and ϕ , integrating over the domain, integrating the pressure gradient term $c^2\nabla\eta$ by parts in the momentum equation, and finally restricting the velocity trial and test functions \mathbf{u} and \mathbf{w} to a finite element subspace $S \subset H(\text{div})$ (where $H(\text{div})$ is the space of square integrable velocity fields whose divergence is also square integrable), and the elevation trial and test functions η and α to the finite element subspace $V \subset L^2$ (where L^2 is the space of square integrable functions):

$$\frac{d}{dt} \int_{\Omega} \mathbf{w}^h \cdot \mathbf{u}^h dV + \int_{\Omega} f \mathbf{w}^h \cdot (\mathbf{u}^h)^\perp dV - c^2 \int_{\Omega} \nabla \cdot \mathbf{w}^h \eta^h dV = 0, \quad \forall \mathbf{w}^h \in S, \quad (3)$$

$$\frac{d}{dt} \int_{\Omega} \alpha^h \eta^h dV + \int_{\Omega} \alpha^h \nabla \cdot \mathbf{u}^h dV = 0, \quad \forall \alpha^h \in V. \quad (4)$$

After discretisation in time, these equations are solved in practise by introducing basis expansions for \mathbf{w}^h , \mathbf{u}^h , η^h , and α^h and solving the resulting matrix-vector systems for the basis coefficients.

In this framework we restrict the choice of finite element spaces S and V so that

$$\mathbf{u}^h \in S \Rightarrow \nabla \cdot \mathbf{u}^h \in V.$$

The divergence should map from S onto V , so that for all functions $\phi^h \in V$ there exists a velocity field $\mathbf{u}^h \in S$ with $\nabla \cdot \mathbf{u}^h = \phi^h$. Such spaces are known as “div-conforming”. Furthermore we require that there exists a “streamfunction” space $E \subset H^1$ such that

$$\psi^h \in E \Rightarrow \mathbf{k} \times \nabla \psi^h \in S,$$

where \mathbf{k} is the normal to the surface, and the $\mathbf{k} \times \nabla$ operator (which we shall write as ∇^\perp) maps onto the kernel of $\nabla \cdot$ in S . A consequence of these properties is that functions in E are continuous, vector fields in S only have continuous normal components and functions in V are discontinuous.

2.2. Energy conservation

Global energy conservation for the linearised equations is a requirement of numerical weather prediction models for various reasons, in particular because it helps to prevent numerical sources of unbalanced fast waves. It is also a precursor to an energy-conserving discretisation of the nonlinear equations using the vector-invariant formulation. For the mixed finite element method, global energy conservation is an immediate consequence of the Galerkin finite element formulation. The conserved energy of Eq. (2) is

$$H = \frac{1}{2} \int_{\Omega} |\mathbf{u}|^2 + c^2 \eta^2 dV.$$

Substituting the solutions \mathbf{u}^h and η^h to Eqs. (3) and (4) and taking the time derivative gives

$$\frac{d}{dt}H = \int_{\Omega} \mathbf{u}^h \cdot \dot{\mathbf{u}}^h + c^2 \eta^h \dot{\eta}^h dV.$$

Choosing $\mathbf{w}^h = \mathbf{u}^h$ and $\alpha^h = \eta^h$ in Eqs. (3) and (4) then gives

$$\frac{d}{dt}H = \int_{\Omega} \mathbf{u}^h \cdot \dot{\mathbf{u}}^h + c^2 \eta^h \dot{\eta}^h dV = \int_{\Omega} \underbrace{-f \mathbf{u}^h \cdot (\mathbf{u}^h)^{\perp}}_{=0} + \underbrace{c^2 \nabla \cdot \mathbf{u}^h \eta^h - c^2 \eta^h \nabla \cdot \mathbf{u}^h}_{=0} dV = 0.$$

2.3. Local mass conservation

Local mass conservation is a requirement for numerical weather prediction models since it prevents spurious sources and sinks of mass. For the nonlinear density equation, this can be achieved using a finite volume or discontinuous Galerkin method. For mixed finite element methods of the type used in this paper applied to the linear equations, consistency and discontinuity of functions in V requires that element indicator functions (i.e., functions that are equal to 1 in one element and 0 in the others) are contained in V . Selecting the element indicator function for element e as the test function α^h in Eq. (4) gives

$$\frac{d}{dt} \int_e \eta^h dV + \int_{\partial e} \mathbf{u}^h \cdot \mathbf{n} dS = 0,$$

where ∂e is the boundary of element e . Since \mathbf{u}^h has continuous normal components on element boundaries, this means that the flux of η^h is continuous and hence η^h is locally conserved.

2.4. Absence of spurious pressure modes and stability of discrete Poisson equation

The principle reason for using the staggered C-grid for numerical weather prediction is that the collocated A-grid, in which pressure and both components of velocity are stored at the same grid locations, suffers from a checkerboard pressure mode which has vanishing numerical gradient when the centred difference approximation is used, despite being oscillatory in space. This pressure mode rapidly pollutes the numerical solution in the presence of nonlinearity, boundary conditions and forcing, and can be easily excited by physics subgrid parameterisations or initialisation via data assimilation from noisy data.

In the context of mixed finite element methods applied to the equation set (2), spurious pressure modes relate to the discretised gradient $D\phi^h \in S$ of a function $\phi^h \in V$ defined by

$$\int_{\Omega} \mathbf{w}^h \cdot D\phi^h dV = - \int_{\Omega} \nabla \cdot \mathbf{w}^h \phi^h dV, \quad \forall \mathbf{w}^h \in S.$$

On uniform grids, spurious pressure modes are functions ϕ^h from the pressure space V which have zero discretised gradient $D\phi^h$ even though $\nabla \phi^h$ is non-zero. On unstructured grids or grids with varying edge lengths, spurious pressure modes are functions which have discretised gradient becoming arbitrarily small as the maximum edge length h_0 tends to zero, despite their actual gradient staying bounded away from zero. Such functions would prevent the numerical solution of Eqs. (2) converging at the optimal rate predicted by approximation theory. We make the following definition of a spurious pressure mode.

Definition 1 (*Spurious pressure modes*). A mixed finite element space (S, V) is said to be free of spurious pressure modes if there exists $\gamma_2 > 0$ independent of h_0 such that for all $\phi^h \in V$, there exists nonzero $\mathbf{v}^h \in S$ satisfying

$$\int_{\Omega} \phi^h \nabla \cdot \mathbf{v}^h dV \geq \gamma_2 \|\phi^h\|_{L_2} \|\mathbf{v}^h\|_{H(\text{div})}. \quad (5)$$

Condition (5) is one of two sufficient conditions for numerical stability of the mixed finite element discretisation of the Poisson equation $-\nabla^2 \phi = f$ given by

$$\begin{aligned} \int_{\Omega} \mathbf{w}^h \cdot \mathbf{v}^h dV &= - \int_{\Omega} \nabla \cdot \mathbf{w}^h \phi^h dV, \quad \forall \mathbf{w}^h \in S, \\ \int_{\Omega} \gamma^h \nabla \cdot \mathbf{v}^h dV &= \int_{\Omega} \gamma^h f^h dV, \quad \forall \gamma^h \in V. \end{aligned}$$

This discretisation is stable (i.e., small changes in the right-hand side lead to small changes in the solution field in the limit as h_0 tends to zero) if Condition (5) holds, together with the condition that there exists $\gamma_1 > 0$ independent of h_0 such that

$$\int_{\Omega} \mathbf{v}^h \cdot \mathbf{v}^h dx \geq \gamma_1 \|\mathbf{v}^h\|_{H(\text{div})}^2 \quad (6)$$

for all $\mathbf{v}^h \in S$ such that $\int \nabla \cdot \mathbf{v}^h \phi^h dV = 0$ for all $\phi^h \in V$. As reviewed in [2], Condition (5) is satisfied if it is possible to define a bounded projection $\Pi^S : H(\text{div}) \rightarrow S$ such that the following diagram commutes:

$$\begin{array}{ccc} H(\text{div}, \Omega) & \xrightarrow{\nabla \cdot} & L_2(\Omega) \\ \downarrow \Pi^S & & \downarrow \Pi^V, \\ S & \xrightarrow{\nabla \cdot} & V \end{array} \quad (7)$$

where Π^V is the usual L_2 projection operator. This means that taking any square integrable velocity field \mathbf{u} with square integrable divergence, evaluating the divergence and projecting into V produces the same result as projecting \mathbf{u} into S using Π^S and evaluating the divergence. The projection Π^S is constructed by applying an L^2 projection of normal components on element edges, ensuring that \mathbf{u} is L^2 -orthogonal to gradients of functions from V in each element, and ensuring the remaining degrees of freedom in \mathbf{u} are L^2 -orthogonal to divergence-free functions in each element. We shall explain how this is done for the two examples described in Section 3. To check that the diagram (7) commutes, it is sufficient to show that

$$\int_K \gamma^h (\nabla \cdot \mathbf{u} - \nabla \cdot \Pi^S \mathbf{u}) dV, \quad \forall \gamma^h \in V, \quad \mathbf{u} \in H(\text{div}, K)$$

for each element K , since this defines the L_2 projection Π^V into the discontinuous space V . This is easily checked using integration by parts:

$$\int_K \gamma^h \nabla \cdot \mathbf{u} dV = - \int_K \nabla \gamma^h \cdot \mathbf{u} dV + \int_{\partial K} \gamma^h \mathbf{u} \cdot \mathbf{n} dS, = - \int_K \nabla \gamma^h \cdot \Pi^S \mathbf{u} dV + \int_{\partial K} \gamma^h \Pi^S \mathbf{u} \cdot \mathbf{n} dS = \int_K \gamma^h \nabla \cdot \Pi^S \mathbf{u} dV$$

as required.

As also reviewed in [2], Condition (6) is satisfied if vector fields $\mathbf{v} \in S$ with divergence orthogonal to V are in fact divergence-free. This is satisfied by the types of mixed finite element methods considered in this paper since the divergence maps from S into V , and so the projection of $\nabla \cdot \mathbf{v}^h$ into V is simply the inclusion. Hence, if the divergence is orthogonal to V , the divergence must be zero, and so (6) is satisfied.

2.5. Discrete Helmholtz decomposition

Proof of the condition that geostrophic modes are steady requires the construction of a discrete Helmholtz decomposition. Since condition (S2) holds, the discrete gradient operator $D : V \rightarrow S$, has only constant functions in the kernel. For any $\psi^h \in E$, the curl ∇^\perp of ψ^h satisfies

$$\int \nabla^\perp \psi^h \cdot D \phi^h dV = - \int \underbrace{\nabla \cdot \nabla^\perp \psi^h}_{=0} \phi^h dV = 0$$

for any $\phi^h \in V$, and hence the curl from E to S and the discrete gradient from V to S map onto orthogonal subspaces of S . This means that there is a one-to-one mapping between elements of S and $E \times V$, defining a discrete Helmholtz decomposition

$$\mathbf{u}^h = \nabla^\perp \psi^h + D \phi^h + \mathbf{h}^h, \quad \mathbf{u} \in S, \quad \psi^h \in E, \quad \phi^h \in V, \quad \mathbf{h}^h \in H, \quad (8)$$

where $H \subset S$ is the space of discrete harmonic velocity fields

$$H^h = \left\{ \mathbf{u}^h \in S : \nabla \cdot \mathbf{u}^h = 0, \quad \int_\Omega \mathbf{u}^h \cdot \nabla^\perp \psi^h dV = 0, \quad \forall \psi^h \in E \right\}.$$

The dimension of H^h is the same as the dimension of the space H of harmonic velocity fields

$$H = \left\{ \mathbf{u} \in H(\text{div}) : \nabla \cdot \mathbf{u} = 0, \quad \int_\Omega \mathbf{u}^h \cdot \nabla^\perp \psi dV = 0, \quad \forall \psi \in H^1 \right\},$$

i.e., velocity fields with vanishing divergence and (weak) curl (in the periodic plane, these harmonic velocity fields are the constant velocity fields, but there are no harmonic velocity fields on the sphere); however $H^h \neq H$ in the general case [4]. The kernel of ∇^\perp in E is the subspace of constant functions, and stability results (as described in Section 2.4) imply that the kernel of D in V is the subspace of constant functions, and hence we can use Eq. (8) to obtain a DOF count for S .

$$\dim(S) = (\dim(E) - 1) + (\dim(V) - 1) + \dim(H),$$

and hence

$$\dim(E) = \dim(S) - \dim(V) + 2 - \dim(H).$$

For our DOF requirement $\dim(S) = 2\dim(V)$, we obtain

$$\dim(E) = \dim(V) + 2 - \dim(H),$$

which becomes $\dim(E) = \dim(V)$ for the periodic plane and $\dim(E) = \dim(V) + 2$ for the sphere. If $\dim(S) > 2\dim(V)$, then $\dim(E) > \dim(V) + (2 - \dim(H))$ and *vice versa*. This will become important when we examine wave propagation in Section 2.8.

2.6. Vorticity and divergence

The discrete vorticity associated with the velocity $\mathbf{u}^h \in S$ is defined as $\xi^h \in E$ such that

$$\int_{\Omega} \gamma^h \xi^h dV = - \int_{\Omega} \nabla^{\perp} \gamma^h \cdot \mathbf{u}^h dV, \quad \forall \gamma^h \in E. \quad (9)$$

It is possible to obtain $\mathbf{u} \in S$ from the discrete vorticity $\xi \in E$ and the divergence $\delta^h = \nabla \cdot \mathbf{u}^h \in V$ by solving two elliptic problems for the streamfunction ψ^h and velocity potential ϕ^h . To obtain the streamfunction $\psi^h \in E$, we use the Helmholtz decomposition and rewrite Eq. (9) as

$$\int_{\Omega} \gamma^h \xi^h dV = - \int_{\Omega} \nabla \xi^h \cdot \nabla \psi^h dV, \quad \forall \gamma^h \in \left\{ \gamma : \gamma \in E, \int_{\Omega} \gamma dV = 0 \right\}, \quad \int_{\Omega} \psi^h dV = 0,$$

which is the usual finite element discretisation of the Poisson equation for ψ^h . To obtain the vector potential ϕ^h requires the solution of the coupled system

$$\begin{aligned} \int_{\Omega} \alpha^h \nabla \cdot D \phi^h dV &= \int_{\Omega} \alpha^h \delta^h dV, \quad \forall \alpha^h \in \left\{ \alpha : \alpha \in V, \int_{\Omega} \alpha dV = 0 \right\}, \\ \int_{\Omega} \mathbf{w}^h \cdot D \phi^h dV &= - \int_{\Omega} \nabla \cdot \mathbf{w}^h \phi^h dV, \quad \forall \mathbf{w}^h \in S, \quad \int_{\Omega} \phi^h dV = 0. \end{aligned}$$

This is the mixed finite element approximation to the Poisson equation

$$\nabla^2 \phi = \delta.$$

If the Brezzi conditions are satisfied due to the existence of the bounded projections defined in Section 2.4, the coupled system is well-posed.

2.7. Steady geostrophic modes

On the f -plane (planar domain with constant f), geostrophic balanced states satisfying $f\mathbf{u}^{\perp} + c^2 \nabla \eta = 0$ are steady since $\nabla \cdot \mathbf{u} = 0$. The remaining solutions of the linear rotating shallow-water equations are fast inertia-gravity waves. In the quasi-geostrophic limit (slow, large scale motion), when nonlinear terms and spatially varying f are introduced, these steady states become slowly-evolving balanced states that characterise large-scale weather systems. It is crucial that a discretisation gives rise to steady geostrophic states on the f -plane, otherwise when nonlinear terms and spherical geometry are introduced, balanced states will emit noisy inertia-gravity waves that will pollute the numerical solution over timescales that are much shorter than that required for a weather forecast. To show that mixed finite element methods have steady geostrophic modes, we follow the approach of [28], namely we aim to show that vanishing divergence implies steady vorticity, then checking that vanishing divergence and steady vorticity implies steady velocity.

To obtain a geostrophic balanced state corresponding to a given streamfunction ψ^h , we initialise \mathbf{u}^h and η^h as follows:

1. Set $\mathbf{u}^h = \nabla^{\perp} \psi^h$.
2. Set η^h from the geostrophic balance relation

$$c^2 \int_{\Omega} \alpha^h \eta^h dV = f \int_{\Omega} D \alpha^h \psi^h dV, \quad \forall \alpha^h \in V. \quad (10)$$

Substitution in Eq. (3) then gives

$$\frac{d}{dt} \int_{\Omega} \mathbf{w}^h \cdot \mathbf{u}^h dV = -f \int_{\Omega} \mathbf{w}^h \cdot \nabla \psi^h dV - c^2 \int_{\Omega} \nabla \cdot \mathbf{w}^h \eta^h dV = f \int_{\Omega} \nabla \cdot \mathbf{w}^h \psi^h dV - c^2 \int_{\Omega} \nabla \cdot \mathbf{w}^h \eta^h dV = 0$$

having noted that $\nabla \cdot \mathbf{w}^h \in V$ and so we may choose $\alpha^h = \nabla \cdot \mathbf{w}^h$ in Eq. (10). To show that $\dot{\eta}^h = 0$, first note that $\mathbf{u}^h = \nabla^{\perp} \psi^h$ and hence $\nabla \cdot \mathbf{u}^h = 0$. Eq. (4) thus becomes

$$\int_{\Omega} \alpha^h \dot{\eta}^h dV = 0, \quad \forall \alpha^h \in V$$

and hence $\dot{\eta}^h = 0$. This means that the geostrophic balanced state is steady.

2.8. Numerical dispersion relations

In this section we consider the numerical wave propagation properties of this family of finite element discretisations, on the f -plane and on the β -plane in the quasi-geostrophic limit.

Dispersion relations are computed by assuming time-harmonic solutions proportional to $e^{-i\omega t}$ (a valid assumption if the equations are invariant under time translations) and studying the resulting eigenvalue problem. For the continuous equations on the periodic plane, the equations are also invariant under spatial translations and so it may be assumed that the eigensolutions take the form $e^{i(\mathbf{k}\cdot\mathbf{x}-\omega t)}$ where \mathbf{k} is restricted so that the periodic boundary conditions are satisfied. Substitution in the equations of motion leads to an algebraic system relating \mathbf{k} to ω : the dispersion relation. For the linear shallow-water equations this system is most easily obtained by using the Helmholtz decomposition for \mathbf{u} . Numerical dispersion relations for continuous-time spatial discretisations are also computed by assuming time-harmonic solutions, leading to a discrete eigenvalue problem. If a structured mesh is used on the periodic plane with a set of discrete translation symmetries then eigensolutions satisfy the property that translating from one cell to another by $\Delta\mathbf{x}$ results in the discrete eigensolution changing by a factor of $e^{i(\mathbf{k}\cdot\Delta\mathbf{x})}$, where \mathbf{k} is again chosen so that the periodic boundary conditions are satisfied. This can again lead to a numerical relationship between \mathbf{k} and ω , obtained for both the f -plane, and the β -plane in the quasi-geostrophic limit, for the hexagonal C-grid in [27], and for the $P1_{DC}$ - $P2$ finite element pair in [12].

Here, we discuss the properties of the discrete eigenvalue problem arising from the finite element spaces from the framework of this paper. The discussion makes use of the discrete Helmholtz decomposition. In the f -plane case, substitution of the discrete Helmholtz decomposition into Eqs. (3) and (4) and assuming time-harmonic solutions yields

$$-i\omega \int_{\Omega} \nabla \gamma^h \cdot \nabla \psi^h dV + \int_{\Omega} f \nabla \gamma^h \cdot D\phi^h dV = 0, \quad (11)$$

$$-i\omega \int_{\Omega} D\alpha^h \cdot D\phi^h dV + \int_{\Omega} f D\alpha^h \cdot \left(\nabla \psi^h + (D\phi^h)^\perp \right) dV - c^2 \int_{\Omega} \nabla \cdot D\alpha^h \eta^h dV = 0, \quad (12)$$

$$-i\omega \int_{\Omega} \alpha^h \eta^h dV + \int_{\Omega} \alpha^h \nabla \cdot D\phi^h dV = 0 \quad (13)$$

for all test functions $\alpha^h \in V$, $\gamma^h \in E$. Next we define projections $P^E : V \rightarrow E$ and $P^V : E \rightarrow V$ by

$$\begin{aligned} \int_{\Omega} \nabla \gamma^h \cdot \nabla (P^E \phi^h) dV &= \int_{\Omega} \nabla \gamma^h \cdot D\phi^h dV, \quad \forall \phi^h \in V, \quad \gamma^h \in E, \\ \int_{\Omega} D\alpha^h \cdot D(P^V \psi^h) dV &= \int_{\Omega} D\alpha^h \cdot \nabla \psi^h dV, \quad \forall \psi^h \in E, \quad \alpha^h \in V. \end{aligned}$$

These projections are uniquely defined since P^E uses the standard continuous finite element discretisation of the Laplace operator which is solvable by the Lax-Milgram theorem when E is restricted to mean zero functions, and P^V uses the mixed finite element discretisation of the Laplace operator using the spaces S and V which is solvable by the Brezzi stability conditions when V is also restricted to mean zero functions.

Using these projections, and the fact that the divergence operator maps from S to V , Eqs. (11)–(13) become

$$-i\omega \psi^h + f P^E \phi^h = 0, \quad (14)$$

$$-i\omega \int_{\Omega} D\alpha^h \cdot D\phi^h dV + f \int_{\Omega} D\alpha^h \cdot D P^V \psi^h dV + \int_{\Omega} f D\alpha^h \cdot (D\phi^h)^\perp dV - c^2 \int_{\Omega} \nabla \cdot D\alpha^h \eta^h dV = 0, \quad (15)$$

$$-i\omega \eta^h + \nabla \cdot D\phi^h = 0 \quad (16)$$

and elimination of ψ^h and use of the definition of D gives

$$\begin{aligned} 0 &= \omega \left((\omega^2 + f^2) \int_{\Omega} \alpha^h \eta^h dV + \int_{\Omega} \alpha^h \eta^h dV - c^2 \int_{\Omega} \nabla \cdot D\alpha^h \eta^h dV \right) + if^2 \int_{\Omega} D\alpha^h \cdot D(P^V P^E \phi^h - \phi^h) dV - \omega \int_{\Omega} f D\alpha^h \\ &\quad \cdot (D\phi^h)^\perp dV, \end{aligned} \quad (17)$$

where ϕ^h is obtained from Eq. (16). The first row of Eq. (17) is the discretisation of the continuous eigenvalue problem for the rotating shallow-water equations using the mixed finite element spaces V and S . In this case the eigenvalues of this discrete eigenvalue problem converge to the eigenvalues of the continuous problem at the optimal rate as described in [5]. However, there are two extra terms in the bottom row of Eq. (17). The second term converges to zero for smooth ϕ^h , and use might be made of spectral perturbation theory to examine what effect this has on the discrete eigenvalue problem; we have not yet developed a technique to do this. However, the impact of the first term in the second row is more immediately clear, since it involves projecting ϕ^h from V to E and back to V again. If V has larger dimension than E , which is the case for the lowest order Raviart–Thomas element on triangles, for example, then this double projection will have a kernel, and $(P^E P^V - 1)\phi^h$ will not be small. This leads to spurious branches of inertia-gravity waves, i.e., branches of solutions of the discrete eigenvalue problem that do not converge to solutions of the continuous eigenvalue problem as $h \rightarrow 0$. See Danilov [14] for numerical

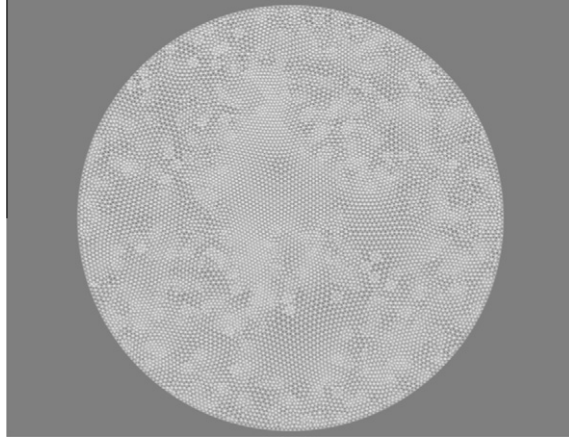


Fig. 2. Mesh used for the Kelvin wave tests.

examples illustrating this spurious modes, in particular Figs. 2–4. Hence, $\dim(V) \leq \dim(E)$ is a necessary condition for the absence of spurious divergent inertia-gravity modes.

A similar approach can be taken to studying the β -plane solutions in the quasi-geostrophic limit. Substitution of the discrete Helmholtz decomposition into equations (3) and (4) and assuming time-harmonic solutions yields

$$-i\omega \int_{\Omega} \nabla \gamma^h \cdot \nabla \psi^h dV + \int_{\Omega} (f_0 + \beta y) \nabla \gamma^h \cdot D\phi^h dV = 0, \quad (18)$$

$$-i\omega \int_{\Omega} D\alpha^h \cdot (D\phi^h + \nabla^{\perp} \psi^h) dV + \int_{\Omega} (f + \beta y) D\alpha^h \cdot \left(\nabla \psi^h + (D\phi^h)^{\perp} \right) dV - c^2 \int_{\Omega} \nabla \cdot D\alpha^h \eta^h dV = 0, \quad (19)$$

$$-i\omega \int_{\Omega} \alpha^h \eta^h dV + \int_{\Omega} \alpha^h \nabla \cdot D\phi^h dV = 0. \quad (20)$$

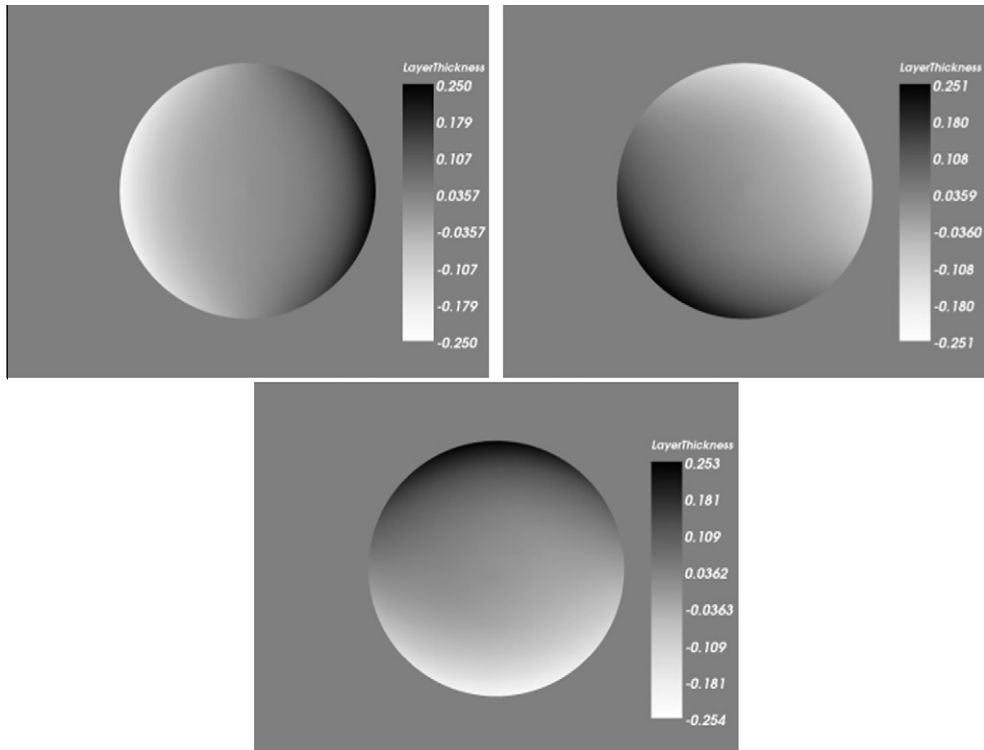


Fig. 3. Snapshots of the free surface elevation for the circular Kelvin wave testcase obtained at times $t = 0, 250,000, 500,000$. The numerical scheme maintains the geostrophic balance in the normal direction, as indicated by the lack of radiated inertia-gravity waves.

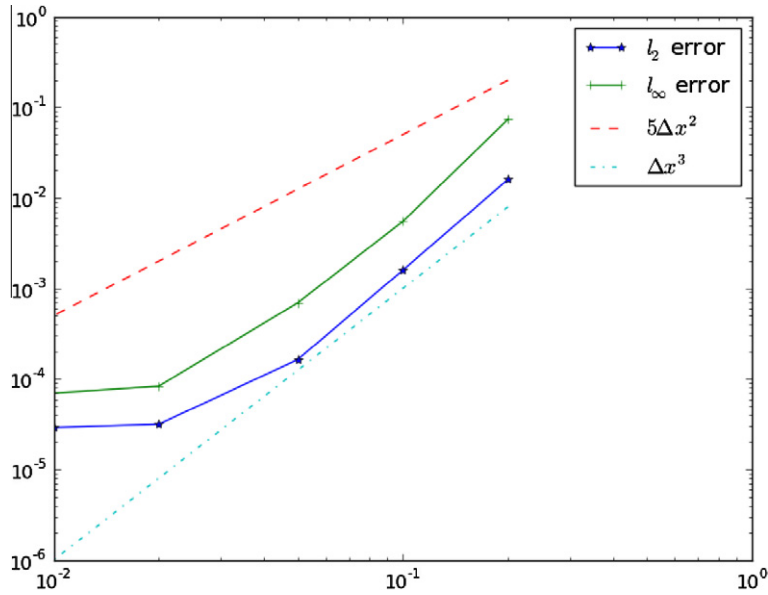


Fig. 4. Plot of errors from the Rossby convergence test with Rossby number $Ro = 1e-3$ and timestep size $\Delta t = 0.007996$. The comparison is made after time $\pi/(1 + 8\pi^2)/2$ after which time the wave has travelled halfway around the domain. For large Δx we observe third-order convergence in both l_2 and l_∞ norms; for smaller Δx the error is dominated by either the timestepping error or the $\mathcal{O}(Ro^2)$ truncation error in the small Rossby number expansion.

In the usual quasi-geostrophic limit, the leading order solution is

$$\phi_g^h = 0, \quad \int_{\Omega} f_0 D\alpha^h \cdot \nabla \psi_g^h dV + c^2 \int_{\Omega} \nabla \cdot D\alpha^h \eta_g^h dV = 0,$$

where ϕ_g^h , ψ_g^h and η_g^h are the leading order terms in the low Rossby number expansion of ϕ^h , ψ^h and η^h respectively. This is the same as the geostrophic steady state formula for the f -plane, and we have

$$f_0 P^V \psi_g^h = c^2 \eta_g^h.$$

The next order in the expansion of the equations (we do not make use of the next order in the ϕ^h equation) is

$$-i\omega \int_{\Omega} \nabla \gamma^h \cdot \nabla \psi_g^h dV + \int_{\Omega} f_0 \nabla \gamma^h \cdot D\phi_{ag}^h dV + \int_{\Omega} \beta y \nabla \gamma^h \cdot \nabla^\perp \psi_g^h dV = 0, \quad (21)$$

$$-i\omega \int_{\Omega} \alpha^h \eta_g^h dV + \int_{\Omega} \alpha^h \nabla \cdot D\phi_{ag}^h dV = 0. \quad (22)$$

Again, the embedding property implies that $i\omega \eta_g^h = \nabla \cdot D\phi_{ag}^h$. Since γ^h is continuous and $D\phi_{ag}^h$ has continuous normal components, we may integrate by parts in the second two terms in Eq. (21), to obtain

$$0 = -i\omega \int_{\Omega} \nabla \gamma^h \cdot \nabla \psi_g^h dV - i\omega \int_{\Omega} \frac{f_0^2}{c^2} \gamma^h \psi_g^h dV - \int_{\Omega} \beta \gamma^h \frac{\partial}{\partial x} \psi_g^h dV + i\omega \int_{\Omega} \frac{f_0^2}{c^2} \gamma^h (1 - P^E P^V) \psi_g^h dV.$$

The first line is the continuous finite element approximation to the Rossby wave eigenvalue problem using the finite element space E , which has convergent eigenvalues. The second line is a perturbation involving $(1 - P^E P^V) \psi_g^h$ which will not always be small if $P^E P^V$ has a non-trivial kernel. This will be the case if $\dim(V) < \dim(E)$, as occurs in the lowest order Brezzi–Douglas–Marini (BDM1) element on triangles [9] which has $P2$ as the streamfunction space, and hence $\dim(E) = \dim(V)/2 + 2 - \dim(H)$. If $P^E P^V$ has a non-trivial kernel, this will lead to spurious Rossby wave branches of the numerical dispersion relation. We conclude that $\dim(V) = \dim(E)$ is a necessary condition for avoiding both spurious divergent modes and spurious irrotational modes. Note that this is not a necessary condition since it is still possible for $P^E P^V$ or $P^V P^E$ to have non-trivial kernel even in this case. This condition motivates the selection of examples of mixed finite element spaces given in the next section.

3. Examples

In this section we provide two examples of mixed finite element spaces that are suitable for constructing pseudo-uniform grids on the sphere, and that have the additional property that there are exactly twice as many velocity degrees of freedom as pressure degrees of freedom, which prevents the presence of spurious mode branches. The first example is the modified

Raviart–Thomas element on quadrilaterals, and the second example is the Brezzi–Douglas–Fortin–Marini element on triangles.

3.1. Modified Raviart–Thomas element on quadrilaterals

There have been several efforts at developing numerical weather prediction models based on a cubed sphere grid (see [21], for example) in which a grid on the surface of a cube is projected to a sphere. The drawback in using such a grid is that to obtain a C-grid finite difference method with stationary geostrophic states, the scheme of Thuburn et al. [28] must be used, which requires the grid to be orthogonal in the sense that lines joining adjacent pressure nodes must cross cell boundaries at right-angles. On the cubed sphere, this condition does not produce a pseudo-uniform grid since elements become clustered near the poles as the resolution is increased. Mixed finite elements provide extra freedom to design numerical schemes since the orthogonality condition is not a requirement; it is replaced by the conditions on finite element spaces specified in Section 2.

The lowest-order Raviart–Thomas finite element space is the mixed finite element analogue of the C-grid since the pressure space is piecewise constant functions, and the velocity fields are constrained to have constant, continuous normal components on element edge. This means that one normal component of velocity must be stored on each element edge, just like the C-grid. The velocity fields are constructed on a square 1×1 reference element \hat{K} with coordinates (ξ_1, ξ_2) , on which the ξ_1 -component of velocity $\hat{\mathbf{u}}$ is obtained by linear interpolation between constant values on the $\xi_1 = 0$ and $\xi_1 = 1$ edges, and the ξ_2 -component is obtained by linear interpolation between constant values on the $\xi_2 = 0$ and $\xi_2 = 1$ edges. In these coordinates, the divergence is constant. In any physical element K in the mesh, we define a coordinate mapping $\mathbf{g} : \xi \mapsto \mathbf{x}$, and the velocity in K is obtained via the Piola transformation

$$\mathbf{u}(\mathbf{x}) = \frac{1}{\det(\frac{\partial \mathbf{g}}{\partial \xi})} \frac{\partial \mathbf{g}}{\partial \xi} \cdot \hat{\mathbf{u}}(\xi),$$

which preserves flux integrals

$$\int_{\gamma} \hat{\mathbf{u}} \cdot \mathbf{n} dS(\xi) = \int_{\mathbf{g}(\gamma)} \mathbf{u} \cdot \mathbf{n} dS(\mathbf{x})$$

guaranteeing continuity of normal fluxes. The divergence satisfies

$$\nabla \cdot \mathbf{u} = \frac{1}{\det(\frac{\partial \mathbf{g}}{\partial \xi})} \hat{\nabla} \cdot \hat{\mathbf{u}},$$

where $\hat{\nabla}$ is the divergence in the local coordinates ξ . If the coordinate transformation is affine (elements are parallelograms), the determinant of the Jacobian is constant, and so the divergence of the velocity is constant in each element. However, for general quadrilateral elements (required for the cubed sphere), the coordinate transformation is bilinear, with linear determinant of the Jacobian. The solution, proposed by Boffi and Gastaldi [6], is to modify the basis functions by adding a divergent correction with vanishing normal components on the boundary that makes the divergence constant. The corresponding streamfunction space E is the usual continuous bilinear space on quadrilaterals, often denoted Q_1 , and it can easily be shown that the ∇^\perp operator maps from E into S in this case. In fact, the Boffi–Gastaldi correction adds a purely divergent component to the velocity field and so the ∇^\perp embedding property is not affected.

The RT0–Q0 finite element space has one pressure degree of freedom per quadrilateral element, and one velocity degree of freedom per edge. Since (for periodic boundary conditions or the sphere) each edge is shared by two elements, this means that there are exactly twice as many velocity degrees of freedom as pressure degrees of freedom. This modified Raviart–Thomas finite element space satisfies all the conditions that we require in this paper and hence has potential for use on pseudo-uniform grids for numerical weather prediction.

3.2. Brezzi–Douglas–Fortin–Marini element on triangles

There is an analogous Raviart–Thomas finite element space on triangles which satisfies the required embedding properties. However, these spaces satisfy $2\dim(V) > \dim(S)$ in general. For example, the lowest order finite element space RT0–P0 has one pressure degree of freedom per element, and one velocity degree of freedom per edge, meaning that $3\dim(V) = 2\dim(S)$. The BDM1 element on triangles has one pressure degree of freedom per element and two velocity degrees of freedom per edge, meaning that $3\dim(V) = \dim(S)$, so $2\dim(V) < \dim(S)$. However, the little-used lowest order Brezzi–Douglas–Fortin–Marini (BDFM1) element together with P_{1D} on triangles satisfies $2\dim(V) = \dim(S)$. The BDFM family of elements for quadrilaterals was introduced in [7], and an analogous family for triangles was described in [8]. On triangles it is infrequently used since the BDM and RT families have less degrees of freedom for the same order of convergence (after suitable post-processing). However, these extra degrees of freedom are useful to us here since they mean that $\dim(V) = \dim(E)$.

Here we describe the BDFM1 element on triangles as an augmentation of the BDM1 element on triangles, which we recall first. Given a triangle K , we define $P_k(K)$ to be the space of k th order polynomials on K . We define the following spaces on K :

$$\begin{aligned} \text{velocity space } S(K) &= \{P_1(K)\}^2, \\ \text{pressure space } V(K) &= P_0(K). \end{aligned}$$

For a triangulation T of the domain Ω , we define the BDM1 velocity space

$$S = \{\mathbf{v} \in H(\text{div}, \Omega) : \mathbf{v}|_K \in S(K), \quad K \in T\},$$

where $H(\text{div}, \Omega)$ is the space of vector fields with square integrable divergence, which requires that \mathbf{v} has continuous normal component across triangle edges. The pressure space is

$$V = \{\eta : \eta|_K \in V(K)\}$$

with no continuity requirements across edges.

A convenient set of local nodal basis functions for S is defined by choosing two node points on each triangle edge, each node located at one of the vertices belonging to that edge: a total of six node points. For example, in the triangle shown in Fig. 1, on edge $e1$ there are two node points, one at vertex $v3$ and one at vertex $v2$. The basis function associated with edge $e1$ and vertex $v3$ is

$$\phi_{1,3} = \mathbf{t}_2 \lambda_3,$$

where \mathbf{t}_2 is the unit tangent vector to edge $e2$ and where $\{\lambda_i\}_{i=1}^3$ are the barycentric coordinates associated with vertices $e1, e2$ and $e3$ respectively. It can easily be checked that $\phi_{1,3}$ has normal component equal to 1 at the node point located at vertex $v3$ on edge $e1$, and normal component equal to zero at each of the other node points. The other six basis functions are constructed in a similar manner.

To increase the number of degrees of freedom in each triangle K in the triangulation T , we define the local BDFM1 space $\hat{S}(K)$ by

$$\hat{S}(K) = \{\mathbf{v} \in P_2(K)^2 : \mathbf{v} \cdot \mathbf{n} = 0 \text{ on } \partial K\}.$$

Since all of the vectors in $\hat{S}(K)$ vanish on the boundary of K , they do not alter the values of the normal components at the boundary, and so there are no additional continuity constraints. The dimension of $P_2(K)^2$ is 12, and there are 9 independent degrees of freedom which do not vanish on the boundary, which means that $\dim(\hat{S}(K)) = 3$.

A convenient set of local nodal basis functions for \hat{S} is defined by locating nodes that store the tangential component of velocity at the centre of each edge. The tangential component of velocity is permitted to be discontinuous and so a different value of the tangential component will be stored on each side of the edge. The basis function associated with the node at the centre of edge $e1$ is

$$\phi_1 = 4\mathbf{t}_1 \lambda_2 \lambda_3.$$

It can easily be checked that ϕ_1 has vanishing normal component on all edges, tangential component equal to 1 at the centre of edge $e1$ and vanishing tangential component on the other two edges. The other two basis functions are constructed in a similar manner.

The augmented velocity space S on the triangulation T is defined as

$$S = \{\mathbf{v} \in H(\text{div}, \Omega) : \mathbf{v} = \mathbf{v}' + \hat{\mathbf{v}}, \mathbf{v}'|_K \in S(K), \quad \hat{\mathbf{v}}|_K \in \hat{S}(K), \quad K \in T\}.$$

The pressure space V is defined as

$$V = \{\eta \in P_1(K)\}$$

with no continuity requirements. For this mixed element pair the velocity space S has 6 DOF per element, and the pressure space V has 3 DOF per element, hence there are twice as many velocity DOF as pressure DOF, just as for the C-grid finite difference method on quadrilaterals.

For our augmented velocity space, it is easy to define the projection operator Π^S . The projection is computed element by element and guarantees the continuity of $\mathbf{u} \cdot \mathbf{n}$ across element edges. The projection on an element K is defined from the following conditions:

$$\int_{e(i)} \gamma^h (\Pi^S \mathbf{u} - \mathbf{u}) \cdot \mathbf{n} dS = 0 \quad \forall \gamma^h \in P^1(e(i)), \quad \forall \text{ edges } e(i) \in \partial K, \quad i = 1, 2, 3, \quad (23)$$

$$\int_K \nabla \gamma^h \cdot (\Pi^S \mathbf{u} - \mathbf{u}) dV = 0 \quad \forall \gamma^h \in P^1(K), \quad (24)$$

$$\int_K \nabla^\perp B \cdot (\Pi^S \mathbf{u} - \mathbf{u}) dV = 0, \quad (25)$$

where B is the cubic ‘‘bubble’’ function (as used in the MINI element [3]). In a triangle K , the cubic bubble function B_K is the unique cubic polynomial which takes the value 1 at the barycentre and 0 on all three edges. The streamfunction space E is

$$E = \{\psi \in H^1(\Omega) : \psi|_K = \psi'|_K + \alpha B_K, \quad \psi'|_K \in P_2(K), \quad \alpha \in \mathbb{R}\}.$$

Eq. (23) comprises the BDM1 projection operator, fixing six degrees of freedom. The components of the extra degrees of freedom $\widehat{S}(K)$ are not affected since they all satisfy $\mathbf{u} \cdot \mathbf{n} = 0$ on ∂K . The vector field $\nabla^\perp B$ lies inside $\widehat{S}(K)$ since it is quadratic (being the skew gradient of a cubic function, B) and has vanishing normal component on ∂K (since B is zero on ∂K). If we construct an orthogonal (relative to the L_2 inner product) decomposition of $\widehat{S}(K)$ into $\nabla^\perp B \oplus \widetilde{S}(K)$ then we see that Eq. (25) only involves the $\nabla^\perp B$ component, and Eq. (24) only involves the remaining two $\widetilde{S}(K)$ components, as

$$\int_K \nabla \gamma^h \cdot \nabla^\perp B dV = - \int_K \underbrace{\nabla^\perp \cdot \nabla \gamma^h}_{=0} B dV + \int_{\partial K} \nabla \gamma^h \cdot \underbrace{\mathbf{n} B}_{=0} dS,$$

because B vanishes on ∂K . The space $\{\mathbf{v} = \nabla \gamma^h, \gamma^h \in P_1(K)\}$ is spanned by constant vector fields, and hence Eq. (24) fixes the two degrees of freedom in $\widetilde{S}(K)$. Bounds on Π^S can be obtained by following the steps of Brezzi et al. [9], since it simply involves L_2 projection onto various moments.

We define the streamfunction space E as the usual Lagrange continuous quadratic space augmented by cubic bubble functions. For any function $\psi \in E$, the curl ∇^\perp maps into S : $\nabla^\perp \psi \in S$. Furthermore, we may define a projection operator $\Pi^E : H^1(\Omega) \rightarrow H(\text{div})$ by

$$\Pi^E \psi(v_i) = \psi(v_i) \forall \text{ vertices } v_i, \quad i = 1, 2, 3,$$

$$\int_{e_i} \Pi^E \psi dS = \int_{e_i} \psi dS, \forall \text{ edges } e_i, i = 1, 2, 3,$$

$$\int_K \Pi^E \psi dV = \int_K \psi dV$$

for each element K . To show that the projections commute with ∇^\perp , i.e., $\Pi^S \nabla^\perp \psi = \nabla^\perp \Pi^E \psi$, we check each of the conditions (23)–(25). Condition (23) becomes

$$\begin{aligned} \int_{e(i)} \gamma^h \nabla^\perp \psi \cdot \mathbf{n} dS &= \int_{e(i)} \gamma^h \nabla \psi \cdot d\mathbf{x}, \\ &= - \int_{e(i)} \psi \nabla \gamma^h d\mathbf{x} + [\gamma^h \psi]_{v_{e(i)}^-}^{v_{e(i)}^+}, \\ &= - \int_{e(i)} \Pi^E \psi \nabla \gamma^h d\mathbf{x} + [\gamma^h \Pi^E \psi]_{v_{e(i)}^-}^{v_{e(i)}^+}, \\ &= \int_{e(i)} \gamma^h \nabla^\perp \Pi^E \psi \cdot \mathbf{n} dS, \quad \forall \gamma^h \in P^1(e(i)), \quad i = 1, 2, 3, \end{aligned} \quad (26)$$

where $v_{e(i)}^\pm$ are the two vertices at either end of edge $e(i)$, and having noted that $\nabla \gamma^h$ is constant for $\gamma^h \in P^1(e(i))$. Condition (24) becomes

$$\begin{aligned} \int_K \nabla \gamma^h \cdot \Pi^S \nabla^\perp \psi dV &= \int_K \nabla \gamma^h \cdot \nabla^\perp \psi dV, \\ &= - \int_K \underbrace{\gamma^h \nabla \cdot \nabla^\perp \psi}_{=0} dV + \int_{\partial K} \gamma^h \nabla^\perp \psi \cdot \mathbf{n} dS, \\ &= \int_K \nabla \gamma^h \cdot \nabla^\perp \Pi^E \psi dV, \quad \forall \gamma^h \in P^1(K), \end{aligned}$$

where we have used Eq. (26). Finally, condition (25) becomes

$$\begin{aligned} \int_K \nabla^\perp B \cdot \Pi^S \nabla^\perp \psi dV &= \int_K \nabla^\perp B \cdot \nabla^\perp \psi dV, \\ &= - \int_K \nabla^2 B \psi dV + \int_{\partial K} \underbrace{\nabla^\perp B \cdot \mathbf{n} \psi}_{=0} dS, \\ &= - \int_K \nabla^2 B \Pi^E \psi dV, \\ &= \int_K \nabla^\perp B \cdot \nabla^\perp \Pi^E \psi dV, \end{aligned}$$

since $\nabla^2 B$ is constant in K and B is zero on ∂K .

Counting global degrees of freedom,

$$\dim(E) = N_{\text{edge}} + N_{\text{vert}} + N_{\text{face}} = 2N_{\text{edge}} + C, \quad \dim(S) = 3N_{\text{face}} + 2N_{\text{edge}}, \quad \dim(V) = 3N_{\text{face}},$$

where C is the Euler characteristic of the domain Ω which is equal to 0 for the doubly-periodic domain and equal to 2 on the sphere. On the sphere there are two extra constraints: namely that the divergence and the vorticity both integrate to zero,

and so in both cases $\dim(E) + \dim(V) = \dim(S)$. Finally, we note that each triangle has three edges which are each shared with one other triangle, and hence $2N_{\text{edge}} = 3N_{\text{face}}$.

4. Numerical results

In this section we illustrate the properties of the BDFM1 finite element space applied to the linear rotating shallow-water equations. The equations were integrated numerically using the implicit midpoint rule, and the resulting discrete system was solved by using hybridisation which is a standard technique for solving elliptic problems (see [8] for a detailed description) in which the continuity constraints on the velocity space are dropped, and are instead enforced in the equation by Lagrange multipliers. It becomes possible to eliminate both the velocity and free surface variables from the matrix equation, leaving a symmetric positive definite system to solve for the Lagrange multipliers. The velocity and free surface variables can then be reconstructed element-by-element. One of the benefits of this approach is that it can be applied when the Coriolis term is present, resulting in a fully implicit treatment of this term. In our numerical tests this system was solved using a direct solver. In the case of BDFM1- $P1_{DG}$, there are three Lagrange multipliers per element.

In the test cases with variable Coriolis parameter f , a continuous piecewise quadratic representation of f was used.

4.1. Steady states for the f -plane

We verified that the geostrophic states are exactly steady on the f -plane for the BDFM1 finite element space by randomly generating streamfunction fields ψ from the streamfunction space S on the same mesh as used for the $P1_{DG}$ - $P2$ finite element pair steady state tests in [13], with streamfunction equal to zero on the boundary. This mesh is a planar unstructured mesh in the x - y plane in a 1×1 square region. The velocity was initialised by setting $\mathbf{u} = \mathbf{k} \times \nabla \psi$ where \mathbf{k} is the unit normal to the domain i.e., $\mathbf{k} = (0, 0, 1)$, and η was obtained by solving the discrete elliptic system

$$\int_{\Omega} \mathbf{w}^h \cdot \mathbf{v}^h dV + \int_{\Omega} c^2 \nabla \cdot \mathbf{w}^h \eta^h dV = 0, \quad (27)$$

$$\int_{\Omega} \alpha^h \nabla \cdot \mathbf{v} dV = \int_{\Omega} D\alpha^h \cdot f(\mathbf{u}^h)^\perp dV \quad (28)$$

with $c^2 = f = 1$. We then integrated the equations forward for arbitrary lengths of time and observed that the layer thickness h and velocity \mathbf{u} remained constant up to machine precision. We also conducted the same experiment on an icosehedral mesh of the unit sphere with $c^2 = f = 1$ (following the “ f -sphere” experiment of Thuburn et al. [28]) and obtained the same result.

4.2. Kelvin waves in a circular basin

Coastal Kelvin waves provide a challenging test since they propagate at the gravity wave speed along the coast but are geostrophically balanced in the direction normal to the coast. We used the Kelvin wave initial condition for a circular basin with unit dimensionless radius as proposed in [16], with $Ro = 0.1$ and $Fr = 1$. We integrated the equations until 10 dimensionless time units with a time step size $\Delta t = 0.01$.

The mesh used for the Kelvin wave calculation is shown in Fig. 2. Some snapshots of the numerical solution are shown in Fig. 3. There are no spurious gravity waves observed, which means that the BDFM1 discretisation is maintaining geostrophic balance in the normal direction as well as the Kelvin wave structure.

4.3. Rossby waves

To verify the convergence of the method we compared against the Rossby wave solution with streamfunction

$$\psi(x, y, t) = \sin(2\pi x) \sin(2\pi(y + \gamma t)), \quad \gamma = \frac{2\pi}{1 + 8\pi^2}$$

in a square domain with nondimensional length 1, with nondimensional wave propagation speed $c = Ro^2$, and non-dimensional Coriolis parameter

$$f = \frac{1 + Ro y}{Ro}$$

and periodic boundary conditions in the x -direction. This is an exact solution of the Rossby wave equation, but is only an asymptotic limit solution of the linearised rotating shallow-water equations as $Ro \rightarrow 0$, with $\mathcal{O}(Ro^2)$ error. This means that for sufficiently small grid width and time step size we expect the $\mathcal{O}(Ro^2)$ error to dominate. The numerical solution was initialised from this streamfunction following the balanced initialisation approach described in Section 4.1. A plot of the error is shown in Fig. 4. We observe $\mathcal{O}(\Delta x^3)$ convergence until the error saturates because of the finite Rossby number. We attribute this third order convergence to the fact that in Section 2.8 the discrete Rossby wave equation was shown to be equal to usual continuous finite element discretisation of the Rossby wave equation using the space E , plus a perturbation. Since E contains

all of the continuous piecewise quadratic functions, we would expect third-order convergence provided that the perturbation converges to zero sufficiently fast (although we do not currently have any estimates for the convergence of the perturbation).

To demonstrate the performance of the numerical scheme on arbitrary manifolds we constructed an unstructured mesh of a cylinder with unit dimensionless radius and dimensionless height equal to 2. The Coriolis parameter was set to $f = (1 + \text{Roz})/\text{Ro}$ and other parameters were kept the same as the planar Rossby wave tests. We call this configuration the “ β ”-tube since it corresponds to a β -plane that has been wrapped into a cylinder. Some plots of the numerical integration of this test case are provided in Fig. 5; no unbalanced motions are visible from the plots.

4.4. Solid rotation on the sphere

To investigate the grid imprinting caused by the finite element scheme, we integrated the linear rotating shallow-water equations on the sphere with initial condition obtained from the streamfunction $\psi = -u_0 \cos \theta$, where θ is the latitude, $u_0 = 2\pi R/(12 \text{ days})$, and $R = 6.37122 \times 10^6$ is the radius of the sphere. The rotation rate $|\Omega|$ was $1/(1 \text{ day})$, and $g = 9.8$. This solution is a steady state solution of the linear equations with varying f because of the cylindrical symmetry; in general we do not expect numerical discretisations which break this symmetry to preserve the steady state.

In our experiment, we used a level 4 icosahedral mesh (each icosahedron edge being subdivided into 8) of the sphere. The velocity and free surface elevation were initialised according to the procedure described in Section 4.1. To measure the deviation from a steady state, the free surface elevation after 10 days of simulation with a timestep of 3600 s was subtracted from the initial condition. Remarkably, as shown in Fig. 6, the errors were almost indistinguishable from round-off error. It turns out that this is because of the mapping used between functions on the sphere, and functions on the icosahedral mesh with flat triangular elements used for the numerical integration. The finite element streamfunction ψ^h was initialised according to $\psi^h = \psi \circ \phi$, where ϕ is the mapping given as follows:

$$\phi(x, y, z) = \left(\left(\frac{R^2 - z^2}{x^2 + y^2} \right)^{1/2} x, \left(\frac{R^2 - z^2}{x^2 + y^2} \right)^{1/2} y, z \right).$$

This mapping preserves the value of z , and rescales x and y onto the sphere. Hence, we obtain $\psi^h = z$, which can be represented exactly in the streamfunction space E . The same mapping is also applied to the finite element representation f^h of the Coriolis parameter f , and we obtain $f^h = 2|\Omega|z$ which can also be represented exactly. Following the balanced initialisation procedure, the finite element free surface elevation field η^h is obtained by projecting the mapping $\eta \circ \phi^{-1}$ into the pressure space V , where η is the continuous balanced free surface elevation. Substitution into the velocity equation gives

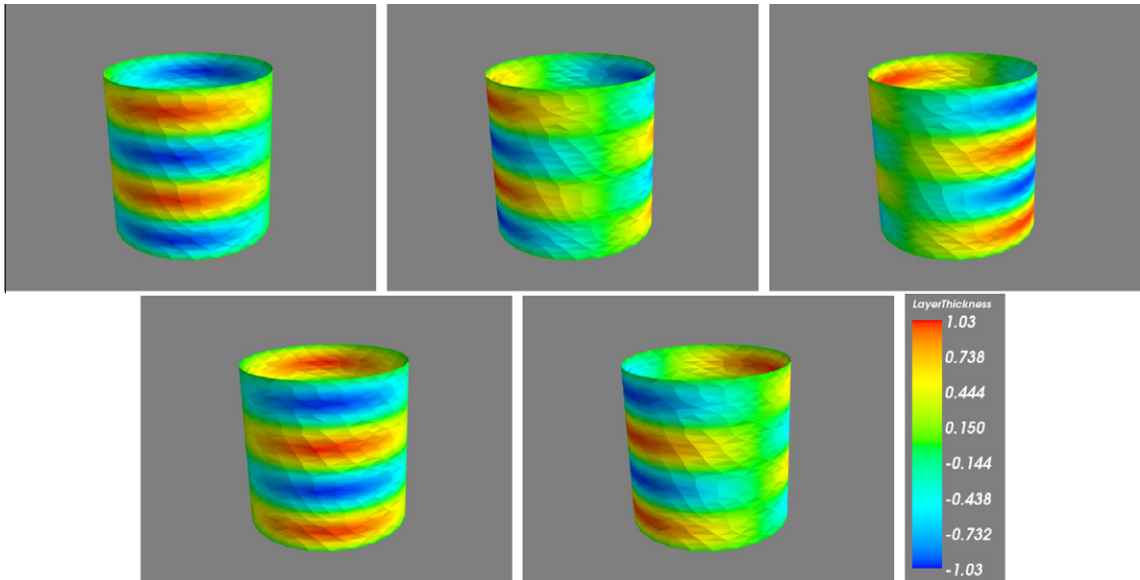


Fig. 5. Rossby waves on the “ β ”-tube initialised from a streamfunction on a cylinder with a coarse unstructured triangle mesh. Colour plots of the free surface elevation are plotted at non-dimensional times $t = 0.79957, 19.9892, 39.9784, 59.9686, 79.9568$ from left to right. No unbalanced motions are visible from the plot.

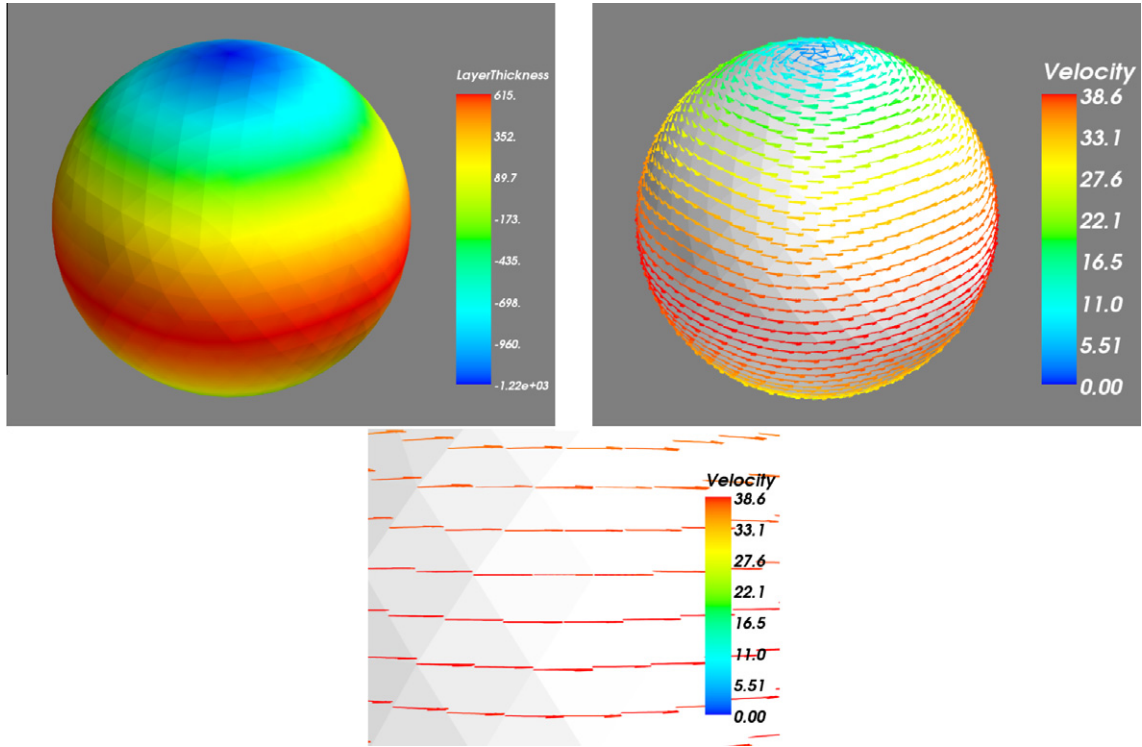


Fig. 6. Plots showing the exact steady numerical solution obtained using the balanced initialisation procedure. Top left: the free surface elevation field. Top right: the velocity field, plotted by evaluating the finite element field at vertices and edge midpoints of each triangle. Since only the normal components are continuous, there are multiple values of these vectors corresponding to the different elements that share those vertices/midpoints. Bottom: Close-up of the velocity vectors near the equator.

$$\begin{aligned} \frac{d}{dt} \int_{\Omega} \mathbf{w}^h \cdot \mathbf{u}^h dV &= - \int_{\Omega} f^h \mathbf{w}^h \cdot (\mathbf{u}^h)^{\perp} dV + c^2 \int_{\Omega} \nabla \cdot \mathbf{w}^h \eta^h dV, \\ [\text{definition of } f^h, \psi^h \text{ and } \eta^h] &= \int_{\Omega} f \mathbf{w}^h \cdot \nabla \psi dV + c^2 \int_{\Omega} \nabla \cdot \mathbf{w}^h \eta dV, \\ [\text{integration by parts}] &= \int_{\Omega} \mathbf{w}^h \cdot \nabla \left(\underbrace{f\psi - c^2\eta}_{=0} \right) dV = 0, \end{aligned}$$

where the second step follows since $\nabla \cdot \mathbf{w}^h \in V$ and so we can use the fact that η^h is a finite element projection of η in V , and where in the last step integration by parts was possible since η is continuous and \mathbf{w}^h has continuous normal components.

5. Summary and outlook

In this paper we described some properties of applying finite element spaces satisfying the div and curl embedding properties, applied to the rotating linear shallow water equations, in order to illustrate their possible suitability for numerical weather prediction on quasi-uniform grids. In this context, these methods can be thought of as more flexible extensions of the mimetic C-grid finite difference method that is currently used in many dynamical cores. This extra flexibility means that non-orthogonal grids and grids with rapid changes of mesh resolution can be used, and the ratio of pressure and velocity degrees of freedom can be adjusted to avoid spurious mode branches. We showed that spurious inertia-gravity mode branches will exist if $\dim(E) < \dim(V)$ and spurious Rossby mode branches will exist if $\dim(V) > \dim(E)$. The discrete Helmholtz decomposition implies that $\dim(E) = \dim(S) - \dim(V) + 2 - \dim(H)$ where H is the space of harmonic velocity fields on the chosen domain. This motivates the search for finite element spaces with $\dim(S) = 2\dim(V)$ that can be used on pseudo-uniform grids on the sphere. In Section 3 we gave two low-order examples: the modified RT0-Q0 element pair for the non-orthogonal cubed sphere, and the BDFM1- $P1_{DG}$ element pair for triangles, the latter of which was illustrated with some numerical examples in Section 4.

In future work, we shall aim to benchmark the augmented mixed element pair in the context of numerical weather prediction and ocean modelling. One of the benefits of this pair is that discontinuous Galerkin methods can be used for the nonlinear continuity equation for the density. These methods are locally conservative, have minimal dispersion and

diffusion errors, and can be made TVB in combination with appropriate slope limiters as described in [10]. Furthermore, as described in [30], if one wishes to have tracer transport that is both conservative and consistent, it is necessary use the pressure space for tracers too. This means that tracer transport can (must) also use the discontinuous Galerkin method.

Finally, we note that although the BDFM(k)-Pk_{DG} finite element spaces do not have a 2:1 ratio of velocity DOFs to pressure DOFs, there does exist a family of higher-order versions of the BDFM1 element pair with a 2:1 ratio, obtained by appropriately augmenting the BDM(k) spaces (with $k > 0$ odd) with higher-order components that vanish on element boundaries. This does not work out so neatly for $k > 1$ since it is also necessary to augment the $P(k)$ space for pressure, to obtain stable element pairs with twice as many velocity DOF as pressure DOF per triangle. In future work, we shall investigate these higher-order element pairs, as well as extensions to tetrahedra in three-dimensions that can be used in unstructured mesh ocean modelling.

Acknowledgements

The authors acknowledge funding from NERC grants NE/I016007/1, NE/I02013X/1, and NE/I000747/1. The shallow water solver was produced using the Imperial College Ocean Model finite element library, unstructured meshes were generated using GMSH, and the icosahedral mesh generator was provided by John Thuburn. Plots were obtained using the Python Matplotlib library and Mayavi2.

References

- [1] A. Arakawa, V. Lamb, Computational design of the basic dynamical processes of the UCLA general circulation model, in: J. Chang (Ed.), *Methods in Computational Physics*, vol. 17, Academic Press, 1977, pp. 173–265.
- [2] D. Arnold, Differential complexes and numerical stability, in: L. Tatsien (Ed.), *Proceedings of the ICM, Beijing 2002*, vol. 1, 2002, pp. 137–157.
- [3] D. Arnold, F. Brezzi, M. Fortin, A stable finite element for the Stokes equations, *CALCOLO* 21 (4) (1984) 337–344.
- [4] D. Arnold, R. Falk, R. Winther, Finite element exterior calculus homological techniques and applications, *Acta Numer.* 15 (2006) 1–155.
- [5] D. Boffi, F. Brezzi, L. Gastaldi, On the convergence of eigenvalues for mixed formulations, *Ann. Scuola Norm. Sup. Pisa Cl. Sci.* XXV (1997) 131–154.
- [6] D. Boffi, L. Gastaldi, Some remarks on quadrilateral mixed finite elements, *Comput. Struct.* 87 (11–12) (2009) 751–757.
- [7] F. Brezzi, On the existence, uniqueness and approximation of saddle point problems arising from Lagrange multipliers, *RAIRO Modél. Math. Anal. Numér.* 8 (1974) 129–151.
- [8] F. Brezzi, J. Douglas, M. Fortin, L. Marini, Efficient rectangular mixed finite elements in two and three space variables, *Modélisation mathématique et analyse numérique* 21 (4) (1987) 581–604.
- [9] F. Brezzi, M. Fortin, *Mixed and Hybrid Finite Element Methods*, Springer-Verlag, 1991.
- [10] F. Brezzi, J.D. Jr, L. Marini, Two families of mixed finite elements for second order elliptic problems, *Numer. Math.* 47 (2) (1985) 217–235.
- [11] B. Cockburn, C.-W. Shu, Runge–Kutta discontinuous Galerkin methods for convection-dominated problems, *J. Sci. Comput.* 16 (3) (2001) 173–261.
- [12] R. Comblen, J. Lambrechts, J.-F. Remacle, V. Legat, Practical evaluation of five partly discontinuous finite element pairs for the non-conservative shallow water equations, *Int. J. Numer. Methods Fluids* 63 (6) (2010) 701–724.
- [13] C. Cotter, D. Ham, Numerical wave propagation for the triangular p1dg-p2 finite element pair, *J. Comput. Phys.* 230 (8) (2011) 2806–2820.
- [14] C.J. Cotter, D.A. Ham, C.C. Pain, A mixed discontinuous/continuous finite element pair for shallow-water ocean modelling, *Ocean Model.* 26 (2009) 86–90.
- [15] S. Danilov, On utility of triangular C-grid type discretization for numerical modeling of large-scale ocean flows, *Ocean Dyn.* 60 (6) (2010) 1361–1369.
- [16] T. Davies, M.J.P. Cullen, A.J. Malcolm, M.H. Mawson, A. Staniforth, A.A. White, N. Wood, A new dynamical core for the Met Office's global and regional modelling of the atmosphere, *Q. J. Roy. Meteor. Soc.* 131 (608) (2005) 1759–1782.
- [17] D.A. Ham, S.C. Kramer, G.S. Stelling, J. Pietrzak, The symmetry and stability of unstructured mesh c-grid shallow water models under the influence of coriolis, *Ocean Model.* 16 (1–2) (2007) 47–60.
- [18] D. Le Roux, V. Rostand, B. Pouliot, Analysis of numerically induced oscillations in 2d finite-element shallow-water models. Part I: Inertia-gravity waves, *SIAM J. Sci. Comput.* 29 (1) (2007) 331–360.
- [19] D. Le Roux, A. Séné, V. Rostand, E. Hanert, On some spurious mode issues in shallow-water models using a linear algebra approach, *Ocean Model.* (2005) 83–94.
- [20] D. Le Roux, A. Staniforth, C.A. Lin, Finite elements for shallow-water equation ocean models, *Mon. Weather Rev.* 126 (7) (1998) 1931–1951.
- [21] D. Majewski, D. Liermann, P. Prohl, B. Ritter, M. Buchhold, T. Hanisch, G. Paul, W. Wergen, J. Baumgardner, The operational global icosahedral-hexagonal gridpoint model GME: description and high-resolution tests, *Mon. Weather Rev.* 130 (2002) 319–338.
- [22] W. Putman, S.-J. Lin, Finite-volume transport on various cubed sphere grids, *J. Comput. Phys.* 227 (2007) 55–78.
- [23] T.D. Ringler, R. Heikes, D. Randall, Modeling the atmospheric general circulation using a spherical geodesic grid: a new class of dynamical cores, *Mon. Weather Rev.* 128 (2000) 2471–2490.
- [24] T.D. Ringler, J. Thuburn, J.B. Klemp, W.C. Skamarock, A unified approach to energy conservation and potential vorticity dynamics for arbitrarily structured C-grids, *J. Comput. Phys.* 229 (9) (2010) 3065–3090, <http://dx.doi.org/10.1016/j.jcp.2009.12.007>.
- [25] V. Rostand, D. Le Roux, Raviart–Thomas and Brezzi–Douglas–Marini finite-element approximations of the shallow-water equations, *Int. J. Numer. Methods Fluids* 57 (8) (2008) 951–976.
- [26] M. Satoh, T. Matsuno, H. Tomita, H. Miura, T. Nasuno, S. Iga, Nonhydrostatic icosahedral atmospheric model (NICAM) for global cloud resolving simulations, *J. Comput. Phys.* 227 (7) (2008) 3486–3514.
- [27] A. Staniforth, Personal communication.
- [28] J. Thuburn, Numerical wave propagation on the hexagonal C-grid, *J. Comput. Phys.* 227 (11) (2008) 5836–5858.
- [29] J. Thuburn, T.D. Ringler, W.C. Skamarock, J.B. Klemp, Numerical representation of geostrophic modes on arbitrarily structured C-grids, *J. Comput. Phys.* 228 (2009) 8321–8335.
- [30] R. Walters, V. Casulli, A robust, finite element model for hydrostatic surface water flows, *Commun. Numer. Methods Eng.* 14 (1998) 931–940.
- [31] L. White, V. Legat, E. Deleersnijder, Tracer conservation for three-dimensional finite element free-surface ocean modeling on moving prismatic meshes, *Mon. Weather Rev.* 136 (2008) 420–442.